Bias-dependent diffusion of a H_2O molecule on metal surfaces by the first-principles method under the grand-canonical ensemble

Satoshi Hagiwara,[1,*] Chunping Hu,[2] Satomichi Nishihara,[2] and Minoru Otani[1,†]

[1]*National Institute of Advanced Industrial Science and Technology (AIST), 1-1-1, Umezono, Tsukuba, Ibaraki 305-8568, Japan*

[2]*AdvanceSoft Corporation, 4-3, Kanda Suruga-dai, Chiyoda-ku, Tokyo 101-0062, Japan*

(Received 18 December 2020; accepted 18 May 2021; published 1 June 2021)

We investigate the process by which a water molecule diffuses on the surface of metal electrodes under constant bias voltage by first-principles density functional theory. In this study, we present the constant electron chemical potential (constant-μ_e) methods combined with the nudged elastic band method. The water diffusion on the Al(111) was calculated using the minimum energy paths (MEPs) for understanding the difference between the constant-μ_e and conventional methods. The simulation shows that the MEP of the water molecule, its adsorption site, and the activation barrier strongly depend on the applied bias voltage. Comparing to the constant total number of electrons (constant-N_e), we found the larger change in the tilted angle of the water dipole in the MEP by the constant-μ_e method. For the comparison between the theoretical results and the previous experiment, we simulate the MEP for a single water diffusion on the Pt(111) surface using constant-μ_e method. When we applied positive bias voltage to the Pt electrode, the result of the activation barrier for a water molecule decreases with increasing the bias voltage, which is consistent with the previous scanning tunneling microscopy (STM) experiment. The proposed constant-μ_e method plays a significant role in understanding the interaction between the electric field and the surface of the material, and is a reliable tool for the simulation of reactions under bias voltage not only using STM but also at the electrochemical interface.

DOI: 10.1103/PhysRevMaterials.5.065001

I. INTRODUCTION

Fundamental studies on metal/water interfaces [1–5] have attracted much attention because understanding the process of water reactions at the interface plays a central role in a wide variety of applications such as catalysis [6] and fuel cells [7]. A recent experiment to investigate the electrochemical interface reportedly showed that the molecular structure of water strongly depends on the electrode potential [8]. Also, an experiment in which scanning tunneling microscopy (STM) was used found that the applied bias voltage affected the activation barrier of water diffusion on a Pt surface [9]. To further understand the water diffusion processes and reactions, it is necessary to clarify the extent to which water adsorption and diffusion on the surface depends on the bias voltage.

First-principles density functional theory (DFT) [10,11] is a powerful tool for investigating the molecular adsorption and diffusion at the surface [12–15]. For the study on the molecular diffusion at the surface, the minimum energy path (MEP) is calculated by the nudged elastic band (NEB) method [16–18]. The details of the MEPs such as the activation barriers and water diffusion structures are useful for understanding the microscopic physical images of the STM observations [19,20]. However, previous theoretical studies on water diffusion processes were mainly carried out without the bias voltage [13,19–24]. Generally, the electrode potential is related to the electron chemical potential (μ_e) of the electrode, and the difference in μ_e between the two subjects defines the bias voltage; the STM tip and metal electrode. Thus, for a system to which a fixed bias voltage is applied, the value of μ_e for the electrode (or sample) surface must be constant. Therefore, to control the bias voltage in the simulation, we need to control μ_e [25–28] beyond the constraint of a fixed number of electrons (constant-N_e).

The quantum mechanical theory formulated under a grand-canonical ensemble is indispensable for a simulation with the fixed μ_e (constant-μ_e) [25–28]. Two flexible simulation methods within the constant-μ_e method have been proposed: The one is the fictitious charge particle (FCP) method developed by Bonnet *et al.* [29], and the other is the grand-canonical self-consistent field (GCSCF) method introduced by Sundararaman *et al.* [30]. These grand-canonical methods based on DFT can be applied not only to the electrochemical interface [30–34] but also to a system subjected to a bias voltage such as in the STM experiment. In the previous studies, however, the constant-μ_e methods have been mainly applied to the electrochemical interface combining with the molecular dynamics [29,31] or implicit solvation theories [30,32–35].

In this study, we carried out a first-principles study on the diffusion processes of a water molecule undergoes on the metal surfaces by varying the bias voltage using the FCP and GCSCF methods. We developed the constant-μ_e methods combined with the NEB method and applied it to the MEPs for a single water diffusion on the metal surfaces. Comparative

*Present address: Center for Computational Sciences, University of Tsukuba, Tsukuba 305-8577, Japan; hagiwara@ccs.tsukuba.ac.jp

†Present address: Center for Computational Sciences, University of Tsukuba, Tsukuba 305-8577, Japan; otani@ccs.tsukuba.ac.jp

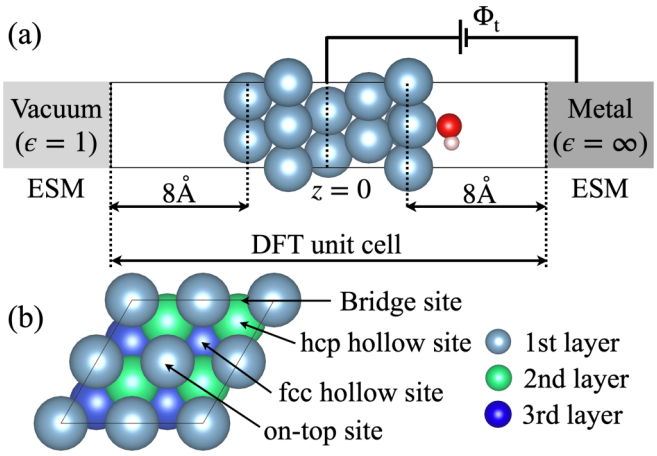

FIG. 1. (a) Schematic view of the model under a bias voltage. The cyan, red, and pink spheres represent Al, O, and H atoms, respectively. The coordinate $z = 0$ is defined as the center of the Al/H_2O system. Two ESM regions with dielectric constants $\epsilon = 1$ and $\epsilon = \infty$, respectively, are attached to the left and right ends of the supercell to represent vacuum and the counter electrode (ESM-metal). (b) Adsorption sites on the Al(111) [or Pt(111)] surface. The cyan, green, and blue spheres represent the first-, second-, and third-layer Al (or Pt) atoms, respectively, counting from the side of the counter electrode.

studies on the present and conventional method were performed by using a single water diffusion on the Al(111). We also simulated the MEPs for a water monomer diffusion on the Pt(111) surface using the constant-μ_e method and compared the results of activation energies to the previous experiment. The paper is organized as follows: Section II provides a brief description of the basic ideas of the constant-μ_e methods, their computational procedures, and the computational details for the DFT and NEB calculations. In Sec. III, we discuss the results obtained by the NEB combined with the constant-μ_e method. Finally, the conclusions of our study are presented in Sec. IV.

II. METHODS AND COMPUTATIONAL DETAILS

Here, we describe the computational methods and details. First, we provide an overview of the constant-μ_e method under the boundary condition of the effective screening medium (ESM) technique [36]. The next subsection presents a discussion of the computational procedures of the FCP and GCSCF methods. Finally, we provide the computational details of the proposed method.

A. Constant-μ_e plus ESM method

First, we briefly describe the basics of the constant-μ_e method combined with the ESM method [36]. The ESM technique, which was developed by Otani and Sugino, is a powerful tool for studying various material surfaces under repeated slab approximation. Figure 1(a) shows a model of a constant-μ_e calculation combined with the ESM used in this study. Two ESM regions with dielectric constants $\epsilon = 1$ and $\epsilon = \infty$, respectively, are attached to the two ends of the supercell to represent the vacuum and the counter electrode (ESM-metal). We modeled the sample surface and STM tip as the surface slab and flat ESM-metal, respectively. Here, the detailed shape of the STM tip is neglected, but we take into account the effect of fixed bias voltage in the water diffusion into the present model using the constant-μ_e method. In this sense, the present model is closer to the experiment compared to the constant-N_e method. Since the electrostatic potential at the ESM-metal boundary was set to zero as the reference potential, the ESM enables us to compare the energies measured from the same reference level.

To achieve the constant-μ_e condition, we use the FCP [29] and GCSCF methods [30]. Both of these methods can be used compute the electronic structure and atomic geometry under the given target chemical potential μ_t. μ_t is imposed by a potentiostat at a potential Φ_t, as shown in Fig. 1(a), i.e., $\mu_t = -e\Phi_t$, where e is the charge of an electron. We can define the grand potential Ω, instead of the total energy functional E_{tot}, as follows:

$$\Omega = E_{tot} - \left(N_e - N_e^0\right)\mu_t = E_{tot} - \Delta N_e \mu_t, \tag{1}$$

where ΔN_e is the total number of the excess charges, which is the difference between the total number of electrons in the system N_e and that in the neutral system N_e^0. Then, we minimize the value of Ω for the atomic positions and ΔN_e, where ΔN_e is not a constant but a dynamic variable during the entire minimization procedure. Because both the FCP and GCSCF methods converge to the same physical state, we expect these two methods to yield the same results under the same computational conditions.

B. Computational procedure of constant-μ_e

Here, we discuss the practical minimization procedure for Ω in the FCP and GCSCF methods. Figures 2(a) and 2(b), respectively, show the flow charts for the calculations with FCP and GCSCF, where we show a series of flows for the DFT calculation with geometry optimization. The SCF and geometry optimization loops show the blue and green shaded areas, respectively. In the following two subsections, we discuss the FCP and GCSCF methods using these flows.

1. FCP method

The FCP employs a grand-canonical ensemble by the system connecting to the fictitious potentiostat, as shown in Fig. 1(a), and minimizes Ω under the constraint of constant-μ_e in the loop in which the geometry is optimized, which is shown as the green shaded area. In the SCF loop shown as the blue shaded area, the Kohn-Sham (KS) equation is solved with the fixed number of electrons. Therefore, the system reaches constant-μ_e via simultaneously optimizing not only the atomic positions but also the total number of electrons N_e. To optimize N_e, we define a fictitious force for N_e as

$$F_e = -\frac{\partial \Omega}{\partial N_e} = -\mu + \mu_t, \tag{2}$$

where, $\mu = \partial E_{tot}/\partial N_e$ implies the instantaneous μ_e, and yields the electrode potential as $\mu = -e\Phi$. To obtain N_e for μ_t, we minimize F_e using the quasi-Newton algorithm by using the Broyden-Fletcher-Goldfarb-Shanno minimization method [37–40]. This method is commonly used for

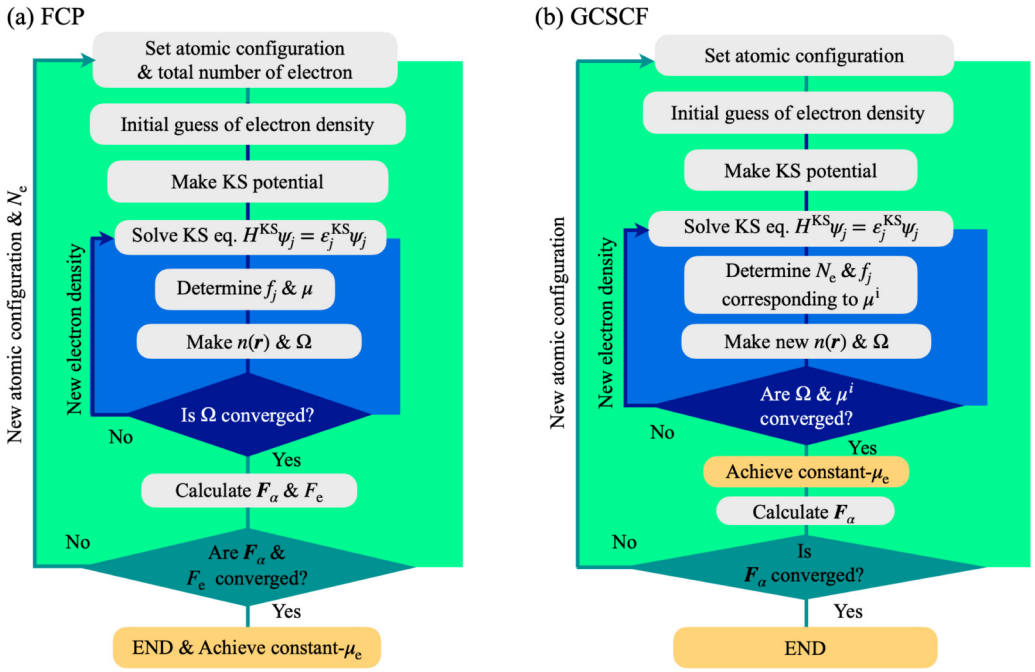

FIG. 2. Calculation flows for (a) FCP and (b) GCSCF methods. The green and blue shaded areas, respectively, indicate the calculation loops for the geometry optimization and self-consistent field. Here, H^{KS}, ε_j^{KS}, and ψ_j denote the Kohn-Sham (KS) Hamiltonian, KS eigenvalue, and KS wave functions, respectively. The electron charge density is obtained by $n(\boldsymbol{r}) = \sum_j f_j|\psi_j(\boldsymbol{r})|^2$, where f_j is the occupation number for each state j. $\boldsymbol{F}_\alpha$ denotes the forces acting on each atom labeled by α.

geometry optimization in conjunction with DFT calculations. In the geometry optimization with the quasi-Newton algorithm, the following equation updates all degrees of freedom for the atomic positions at the k-th iteration ($\boldsymbol{x}_k$), until all forces acting on the atoms become zero, as follows:

$$\boldsymbol{x}_{k+1} = \boldsymbol{x}_k + \boldsymbol{h}_k \boldsymbol{f}_k. \tag{3}$$

Here, $\boldsymbol{f}_k$ and $\boldsymbol{h}_k$ denote the forces acting on the atoms and Hessian, respectively. In conventional geometry optimization, the motion of N atoms in three dimensions produces $3N$ degrees of freedom. In the FCP, both F_e and N_e are included in $\boldsymbol{f}_k$ and $\boldsymbol{x}_k$, respectively. Thus, we explore the solution of Eq. (3) within the space of the $3N+1$-th dimension. However, we cannot directly treat F_e and N_e on equal footing with $\boldsymbol{f}_k$ and $\boldsymbol{x}_k$ because the units of N_e and F_e are different from the atomic positions and forces. To address this, we introduce the effective charge position ($N'_e = \alpha N_e$), where α is a scaling factor unit in bohr/e. F_e is also scaled by α as follows:

$$F'_e = (-\mu + \mu_t)/\alpha. \tag{4}$$

Here, the definition of α is $\alpha = L_{max}/V_{max}C_0$. L_{max} and V_{max} are the upper bound of the change in the length and voltage at each step, respectively. C_0 is the capacitance determined by the formula of the parallel-plate capacitor:

$$C_0 = \frac{1}{4\pi}\frac{S}{L}. \tag{5}$$

Here, S denotes the surface area. Although the original definition of L is the distance between the parallel plates of the capacitor, we approximately use the half-length of the unit cell in the z direction for convenience. In the FCP optimization, we add N'_e and F'_e to $\boldsymbol{x}_k$ and $\boldsymbol{f}_k$, respectively.

In Eq. (3), $\boldsymbol{h}_k$ plays a role in determining the step width of not only the new atomic positions but also the new charge N_e. For the Hessian component of N_e, we use the first derivative of μ with respect to the excess charge ($-\partial\mu/\partial N_e$). In the present implementation, we use the approximate inverse of the density of states (DOS) at μ for $-\partial\mu/\partial N_e$ ($1/\rho(\mu)$). Generally, for a large DOS system near μ_t, μ gradually approaches μ_t because of the small Hessian for N_e evaluated by $1/\rho(\mu)$. Thus, the convergence behavior of the FCP method depends on the DOS near μ_t.

2. GCSCF method

Here, we briefly review the GCSCF method discussed in Ref. [30]. The GCSCF reaches constant-μ_e during the SCF loop, and is shown as the blue shaded area in Fig. 2. Because the formulation of GCSCF is simple, its calculation flow is essentially the same as that of the conventional DFT with geometry optimization. However, in the GCSCF, N_e is a variable at each SCF step. Generally, we can evaluate N_e by summing the occupied KS orbitals with the given μ_t. However, such a simple method for evaluating N_e violates the numerical stability of the SCF [25]. Therefore, it is necessary to modify the numerical algorithms to determine the i-th transient Fermi energy (μ^i) and update the electron density during the SCF loop.

Now, we explain the algorithm for determining the μ^i. In the GCSCF, we gradually approach μ^i to μ_t during the SCF as follows: First, we evaluate the Fermi energy ε_F^i at the i-th SCF step by the total number of electrons at the i-th SCF step, using an ordinal method. Second, μ^i is determined by simply

mixing $\varepsilon_{\mathrm{F}}^{i}$ and μ_{t} as follows:

$$\mu^{i} = \beta\mu_{\mathrm{t}} + (1-\beta)\varepsilon_{\mathrm{F}}^{i}, \tag{6}$$

where β is the mixing factor for μ_{e} ($0 < \beta < 1$). Then, the total number of electrons corresponding to μ^{i} is determined, and we finally update the occupation number and the electron density using μ^{i} and the total number of electrons.

Next, we discuss the charge mixing method using the direct inversion of the iterative subspace (DIIS) method [41] within the GCSCF framework. At the i-th SCF step, we update the electron density by solving the KS equation with an input electron density n_{in}^{i}, and then the updated electron density is used as a n_{in}^{i+1}. However, to obtain a more appropriate value of n_{in}^{i+1}, the updated electron density is mixed with the electron density of the previous SCF steps. To accelerate the convergence of the SCF, we usually use the optimized electron density obtained by the solution of the DIIS method as n_{in}^{i+1}. Usually, to stabilize the DIIS acceleration, the metric and Kerker preconditioning operators [42] $\hat{M}$ and $\hat{K}$ are introduced, and the DIIS method updates the electron density without altering the term of $n(\boldsymbol{G}=\boldsymbol{0})$, where $\boldsymbol{G}$ is the reciprocal lattice vector. In contrast, the GCSCF requires the total number of electrons to be updated in the SCF loop. Thus, we need to update the $n(\boldsymbol{G}=\boldsymbol{0})$ term that corresponds to the total number of electrons in the system by each SCF step. However, the conventional formulation of $\hat{M}$ and $\hat{K}$ used in the ordinal DFT excludes for the terms at $\boldsymbol{G}=\boldsymbol{0}$ because of holding the total number of electrons. Therefore, to stably update N_{e}, we, respectively, introduce the dumping factors of Q_{K} and Q_{M} (>0) to $\hat{K}$ and $\hat{M}$ as follows:

$$\langle \boldsymbol{G}|\hat{K}|\boldsymbol{G}\rangle = \frac{|\boldsymbol{G}|^2 + Q_{\mathrm{K}}^2}{|\boldsymbol{G}|^2 + q_{\mathrm{K}}^2 + Q_{\mathrm{K}}^2}, \tag{7}$$

$$\langle \boldsymbol{G}|\hat{M}|\boldsymbol{G}\rangle = \frac{4\pi}{|\boldsymbol{G}|^2 + Q_{\mathrm{M}}^2}. \tag{8}$$

Here, q_{K} is the original damping factor of the Kerker preconditioning operator. When Q_{K} and Q_{M} are set to zero, $\hat{K}$ and $\hat{M}$ revert to their original values. By introducing Q_{K} and Q_{M}, $\hat{K}$ and $\hat{M}$ at $\boldsymbol{G}=\boldsymbol{0}$ becomes a finite value, and we can always update the total number of electrons in the SCF loop. Once both Ω and μ^{i} have converged, the ordinal geometry optimization procedure provides the new atomic positions.

3. NEB method combined with constant-μ_{e}

Here, we briefly discuss the NEB method in combination with the constant-μ_{e} methods. The NEB method [16–18] describes the MEP for a chemical reaction by combining the images of the first and final states. The MEP is determined by solving Eq. (3) until the forces acting on each image become zero. Thus, in the conventional NEB method, we explore the solution of Eq. (3) within the space of the $3N\times N_{\mathrm{im}}$ dimension, which corresponds to the motion of N atoms in three dimensions with N_{im} images of the MEP. In the NEB combined with the FCP, Eq. (3) is solved within the $(3N+1)\times N_{\mathrm{im}}$ dimension because we extended the optimization space, as discussed in the previous section. In contrast, when used in combination with the GCSCF, the NEB does not require special modification of the optimization procedure for the conventional NEB framework because of its straightforward formulation. In this work, we employ the Broyden method [43] as a quasi-Newton algorithm for determining the MEPs.

C. Computational details

Here, we provide the computational details of this study. All spin-unpolarized calculations were performed using the QUANTUM ESPRESSO package [44,45], which is a DFT code within the plane-wave basis sets and the ultrasoft-pseudopotential [46] framework. We implemented the FCP and GCSCF routines in combination with the ESM method in the package. We used the five-layered slab model in the p(2×2) and the three-layered slab model in the p(4×4) supercells to represent the Al(111) and Pt(111) surfaces with a single water molecule, respectively. The coverages of the water molecule on the Al(111) and Pt(111) slabs used in this study, respectively, correspond to the 0.25 and 0.0625 monolayer. The former is used in previous theoretical studies [12–15,22], and the latter is close to the previous experimental conditions discussed in Ref. [9]. As a representative of the slab models, we show the H_2O adsorbed Al(111) in Fig. 1(a). The two ESM regions with $\epsilon = 1$ and $\epsilon = \infty$ are located at a distance of ∼8 Å from the outermost Al (or Pt) layers.

For convenience, the experimental lattice constants of the face-centered-cubic Al and Pt bulks (4.05×4.05×4.05 Å^3 and 3.925×3.925×3.925 Å^3) [47,48] were used to construct the surface slabs, respectively. For the Al slab, the cut-off energies for the wave functions and charge density were 40y and 320 Ry, respectively. The exchange-correlation term was described by the Perdew–Wang 91 functional within the generalized-gradient approximation [49]. $\boldsymbol{k}$-point sampling used a 5×5×1 mesh in the surface Brillouin zone. For the Pt slab, to increase computational accuracy, we used 60 and 480 Ry as the cut-off energies for the wave functions and charge density, respectively. The van der Waals exchange correlation functional of the vdW-DF2-B86R type [50] was used, and $\boldsymbol{k}$-point sampling was a 3×3×1 mesh in the surface Brillouin zone. The number of electrons occupying the volume was determined by the Gaussian smearing method with a smearing width of 0.01 Ry for all calculations. We carried out the structural optimization until $\boldsymbol{F}_{\alpha} < 5.0\times10^{-4}$Ry/Bohr with the bottom of three Al layers (or a single Pt layer) fixed at bulk truncated positions. In the FCP calculation, the convergence thresholds for Ω and F_{e}, respectively, are set to 1.0×10^{-6} Ry and 1.0×10^{-2} eV. In the GCSCF calculation, we decrease the threshold of the convergence criteria for Ω to 1.0×10^{-8} Ry, and used the Thomas-Fermi charge-mixing method [51].

The NEB [16–18] calculation under the constant-μ_{e} condition, which enables the determination of the MEP between two stable endpoints, was carried out to determine the activation barriers and diffusion paths of H_2O molecules at the surface. The NEB calculation was conducted with ten (nine) discrete images for the MEP of H_2O diffusion on Al(111) [Pt(111)] with a path threshold of 0.03 eV/Å. We allowed to relax the H_2O molecule and two slab layers from the H_2O adsorbed surfaces. The activation barriers and diffusion paths converged well for the number of images and path threshold.

TABLE I. The activation energies E_a (in eV) of H_2O diffusion on the Al(111) under bias voltages of $U = 0.0$ V, -1.0 V, and $+1.0$ V using the constant-μ_e method. The results of E_a for the constant-N_e method with and without ΔQ_e are also listed. The superscripts of E_a by the constant-μ_e method, respectively, denote the results obtained by the FCP and GCSCF methods.

	Constant-μ_e		Constant-N_e	
U	E_a^{FCP}	E_a^{GCSCF}	ΔQ_e	E_a
0.0 V	0.092	0.091	0.000e	0.143
-1.0 V	0.161	0.161	$+0.033e$	0.184
$+1.0$ V	0.024	0.028	$-0.036e$	0.095

III. RESULTS AND DISCUSSIONS

First, we discuss the results of water adsorption and diffusion on the Al(111) surface as calculated using the NEB method with constant-μ_e. Here, we aim to check the present implementation of the constant-μ_e and to understand differences in the results between the constant-μ_e and -N_e methods. Finally, we compare the results for the bias-voltage dependence of water diffusion on the Pt(111) to the previous STM observation.

A. Adsorption site of water-molecule on Al(111)

First, we briefly discuss the adsorption energy and μ_e at the neutral Al(111) surface with a H_2O molecule for adsorption sites, as shown in Fig. 1(b). The calculation shows that the on-top sites are the most stable for H_2O adsorption, and the adsorption energy we obtained for these sites is 0.23 eV. These results are consistent with the previous DFT result [22]. For the MEP, we considered H_2O diffusion from one stable on-top site to the next on-top site via a bridge site [52]. To apply the bias voltage U, we measure μ_t from μ_e at the potential of zero charges (PZC), μ_{PZC}, which was -2.91eV relative to the reference electrode level. Here, μ_{PZC} was determined as the chemical potential of an ordinary DFT calculation at zero excess charges (ΔQ_e). The value of U is defined as $U = (\mu_t - \mu_{PZC})/e$ [53], and the three values of U are examined: $U =$ 0V, -1V, and $+1$V, respectively.

For comparative study, we also carried out the constant-N_e calculations using values of ΔQ_e obtained by the constant-μ_e calculations of the H_2O adsorbed surfaces for the first images of the NEB. The results obtained for ΔQ_e under $U = -1$V and $U = +1$V are $+0.033e$ and $-0.036e$, respectively. The difference in the absolute values of ΔQ_e between $U = 1$V and -1V implies that the response of surface electrons to the applied bias potential deviates from the linear response regime. Notably, we employ ΔQ_e obtained above for the following constant-N_e calculations.

B. Activation barrier of water-diffusion on Al(111)

Table I presents the results of the activation barriers E_a obtained by the NEB with the constant-μ_e and -N_e methods. First, we briefly compare the E_a obtained by the FCP and GCSCF methods (E_a^{FCP} and E_a^{GCSCF}). The results of E_a^{FCP} are almost the same as those of E_a^{GCSCF}. Because the FCP and GCSCF methods converge to the same physical state, this agreement between the methods is reasonable. Hereafter, unless otherwise specified, we discuss the results of E_a using those derived with FCP as being representative of the constant-μ_e method.

The result of E_a for the constant-N_e with $\Delta Q_e = 0.000e$ is very close to that of the previous climbing image NEB [22]. In contrast, constant-μ_e with $U = 0.0$ V produces a much lower E_a compared to E_a by the constant-N_e with $\Delta Q_e = 0.000e$. Under $U = -1.0$ V, E_a increases to 0.161 eV, which is also smaller than the counterpart value of 0.184 eV obtained with the constant-N_e method with $\Delta Q_e = +0.033e$. By switching the value of U from 0.0 V to $+1.0$ V, E_a decreases from 0.092 to 0.024 eV. E_a with $U = +1.0$ V is still lower than that determined by using the constant-N_e method with $\Delta Q_e = -0.036e$. The above comparison between the constant-μ_e and -N_e methods shows that although they yield similar trends for E_a either as a result of applying bias voltages or introducing excess charges, the results are quantitatively quite different.

C. MEPs for water-diffusion on Al(111)

Here, we discuss the results of the water diffusion path obtained by the NEB with the constant-μ_e and -N_e methods. Figures 3(a)–3(c), respectively, show consecutive images of the water diffusion along the MEPs at applied bias voltage of $U = 0$ V, $+1.0$ V, and -1.0 V. We also show the results of the direction of the H_2O dipole by obtaining the tilt angle between the dipole normal and the surface (θ_{dip}) along with the diffusion path in Fig. 4(a). Here, we show the results obtained by the FCP as a representative example, because the GCSCF and FCP provide the converged results for the images as shown in Fig. 4(a).

Among the ten MEP images of H_2O, we regard the first and last images as identical, and the water molecules are bonded to the surface Al atom via the O atom. Along the diffusion path, the applied bias voltage drastically alters the dipole direction of the water molecule. As seen in Fig. 4(a), for overall, the change in θ_{dip} becomes smaller for the lower bias voltage. For the first H_2O image, the changes in the adsorption structure of H_2O resulting from the bias voltage are small for the first images of MEPs. However, the value of θ_{dip} changes drastically in the intermediate images. The dipole direction near the bridge site at $U = 0.0$ V and $+1.0$ V becomes nearly perpendicular to the Al surface, and the H atoms orientate themselves downward. In contrast, the dipole directions for all images tend to be parallel to the surface at $U = -1.0$ V. We will discuss an interpretation of bias voltage dependence of the change in θ_{dip} in the next subsection. As a comparative study, Figs. 3(d)–3(f) shows the results obtained for the MEP with the constant-N_e method. Here, the first and last images of H_2O in Figs. 3(d)–3(f) are the same as those in Figs. 3(a)–3(c), respectively. However, the changes in θ_{dip} in the intermediate images are much smaller than those in the constant-μ_e, which is clearly seen in the comparison between Figs. 4(a) and 4(b). Thus, we interpret the difference in the results of E_a between the constant-μ_e and -N_e, as presented in Table I, as the difference in the MEPs. Therefore, this result of the H_2O geometry along the MEPs denotes that the presence of the fixed bias voltage plays an important role to understand the diffusion process on the surface.

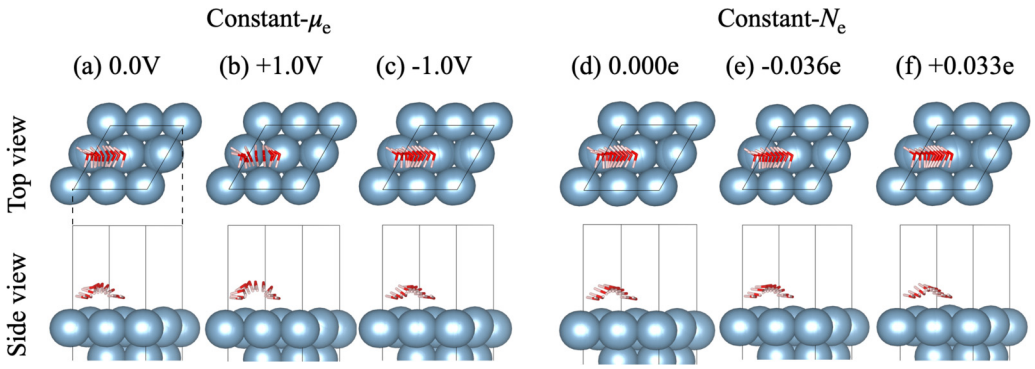

FIG. 3. Consecutive views of the MEP (ten images) for water diffusion on Al(111): results of constant-μ_e method with bias-voltages of (a) 0.0 V, (b) +1.0 V, (c) −1.0 V, and constant-N_e method with the excess charge of (d) 0.000e, (e) −0.036e, and (f) +0.033e. The cyan, pink, and red spheres represent Al, H, and O atoms, respectively. The upper and lower panels show top and side views of the calculation cell, respectively.

D. Details of H_2O diffusion along the MEPs

Figure 5 shows the results of the analysis for the MEPs. Before discussing the details of the diffusion properties, we briefly discuss the results between the FCP and GCSCF methods shown in Figs. 5(a) and 5(c). Overall, the results of changes in the grand-potential ($\Delta\Omega$) and ΔQ_e along the MEPs obtained by the FCP (represented by open circles) and GCSCF (represented by cross symbols) are the same within the computational accuracy. These results indicate that we successfully implemented the constant-μ_e methods. The main difference between the FCP and GCSCF methods is the computational procedure discussed in Sec. II. Because, as discussed above, we used the extended Hessian in the FCP method, the convergence behavior depends on the inverse of the DOS near μ_t. In contrast, the GCSCF method directly optimizes μ_e during a single SCF calculation. Because these constant-μ_e methods employ different optimization procedures, we need to consider a different strategy to develop the FCP and GCSCF methods to more efficiently reach the constant-μ_e condition.

Figure 5(a) presents the results of $\Delta\Omega$, where the black, red, and blue circles, respectively, denote the values under $U = 0.0$ V, −1.0 V, and +1.0 V. In terms of the overall trend, the heights of $\Delta\Omega$ reach their respective maximum values in the intermediate images and decrease with increasing bias voltage. This behavior indicates that E_a of the diffusion of water on Al(111) depends on the bias voltage, as listed in Table I. For $U = +1.0$ V, we found negative values of $\Delta\Omega$ at intermediate images of the diffusion path. This result indicates that the stable adsorption sites of the H_2O molecules on Al(111) change from the on-top sites to sites in the vicinity of the bridge sites. The result of E_a at $U = +1.0$ V measured from bottom of the MEP is 0.043 eV, whose value is still smaller than that at $U = 0.0$ V. Thus, the change in the stable adsorption site does not alter the qualitative feature of the bias-voltage dependence of the E_a discussed in Table I. In contrast, the results of ΔE_{tot} shown in Fig. 5(b) obtained by the constant-N_e method do not alter the sign of ΔE_{tot} for any values of ΔQ_e. Therefore, a comparison of the results of the constant-μ_e and -N_e methods would necessitate careful adjustment of the bias voltage to determine the stable adsorption site of H_2O on Al(111) in the STM experiments and at the electrochemical interface.

Figure 5(c) shows the results of the change in the ΔQ_e introduced by a potentiostat along the diffusion pathway. In the first images, the values of ΔQ_e are the same as those used in the constant-N_e calculations. In the next few images, the value of ΔQ_e slightly increases, and then it decreases in the intermediate images of the MEPs. This result is the consequence of introducing excess charges from an external potentiostat to Al(111) to maintain a constant bias voltage. Resulting from the introduced ΔQ_e, the electrode surface becomes negatively charged around the intermediate images. Since ΔQ_e enhances the attractive (repulsive) Coulomb interaction between H (or O) atoms and electrode surface, the change in the θ_{dip} around the intermediate image becomes large shown in Fig. 4(a). When the bias voltage is increased, the values of ΔQ_e shift towards more negative. Therefore, the bias voltage dependence of θ_{dip} comes from the enhanced attractive Coulomb interaction between the H atoms and electrode by ΔQ_e. On the other hand, the results obtained for $\Delta\mu_e$ by using the constant-N_e method highly depend on the MEPs shown in Fig. 5(d). Here, we define $\Delta\mu_e$ as the difference between the μ_es in the MEPs and that in the first image of the MEPs of the PZC. Thus, $\Delta\mu_e$ corresponds to the bias voltage of the electrode. Because the total number of electrons is fixed, this result originates from the charge transfer between the H_2O adsorbate and the Al electrode. Therefore, the change in the surface dipole barrier alters the work function, which leads to the dependence of $\Delta\mu_e$ on the H_2O diffusion path. $\Delta\mu_e$ around the intermediate images tends to decrease from that at the first image. Thus, the bias voltage for the electrode decreases during the water diffusion, which reduces the interaction between the water dipole and electric field. For this reason, the constant-N_e method predicts the slight change in the θ_{dip} comparing to that by constant-μ_e shown in Figs. 3 and 4. As discussed above, these differences in the control mechanism of the surface charge between the constant-μ_e and -N_e methods provide the different MEPs for H_2O diffusion at Al(111).

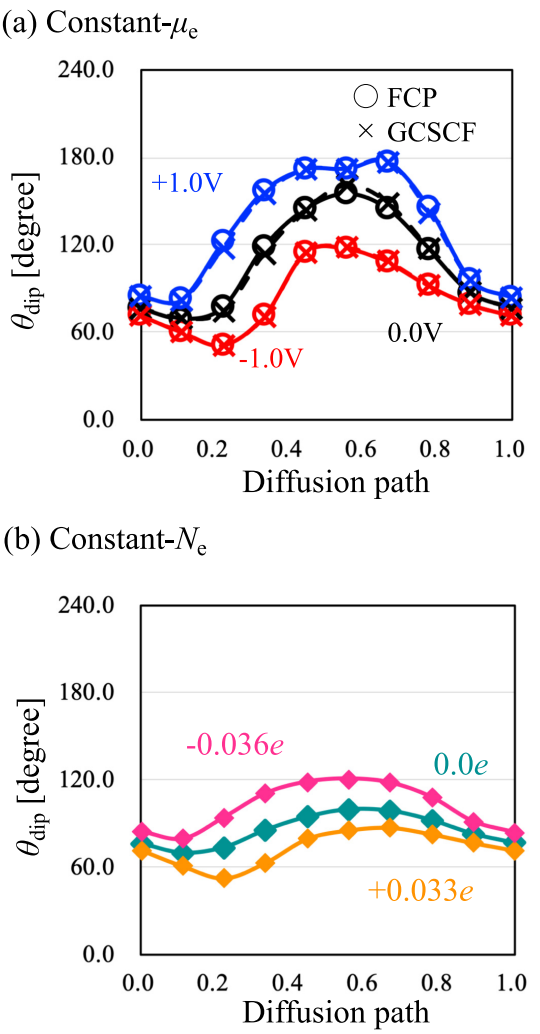

FIG. 4. Dipole angle of the water molecule on the Al(111) (θ_{dip}) along with the diffusion path obtained by (a) constant-μ_e and (b) constant-N_e methods. The black, red, and blue symbols are θ_{dip} with bias-voltages of 0.0 V, −1.0 V, and +1.0 V, respectively. The open circles denotes the results obtained by the FCP method, and the cross symbols stand for the results obtained by the GCSCF method. The green, orange, and pink diamond symbols indicate the results of θ_{dip} with excess charges of 0.0e, +0.033e, and −0.036e, respectively. The solid and dashed lines are intended to guide the eyes.

E. Water-diffusion on Pt(111) surface

Finally, we compare the results of bias-voltage dependence of the water diffusion on Pt(111) surface to the previous STM measurements. We also assumed the water diffusion from the most stable on-top site to the next nearest on-top site via the bridge site. Here, we adopted the FCP method as the constant-μ_e method. According to the previous theoretical studies [19,20], it is necessary to consider the quantum effect such as zero-point vibration energy (E_{ZP}) to calculate the water diffusion on the surfaces more accurately. Therefore, we carried out the vibration analysis for the water on Pt(111) in the initial and transient states of the MEP images using the finite displacement method within the harmonic approximation [54].

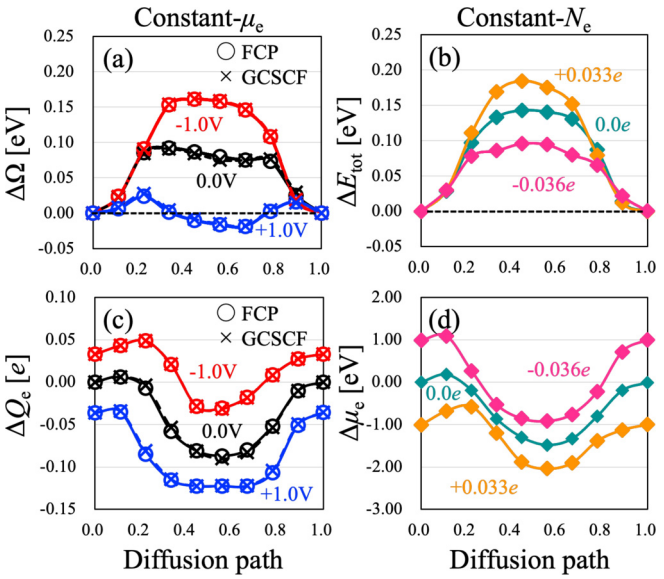

FIG. 5. Changes in the (a) grand-potential $\Delta\Omega$, (b) total energies ΔE_{tot}, (c) introduced excess charges ΔQ_e, and (d) chemical potential $\Delta\mu_e$ as a function of the H_2O diffusion path. The results of (a) and (c) are obtained under $U = 0.0$ V, −1.0 V, and +1.0 V, and the results of (a) and (d) are obtained with $\Delta Q_e = 0.000e$, +0.033e, and −0.036e. The open circles and cross symbols denote the results obtained by the FCP and GCSCF methods, respectively. The results of constant-N_e are represented by diamond symbols. The solid and dashed lines are intended to guide the eyes.

Figure 6 shows the bias-voltage dependence of the E_a obtained by the NEB calculation. The results of E_a without the correction of E_{ZP} (cross symbols) decrease with increasing bias-voltage. This result is similar to the bias-voltage dependence of E_a for a single water-diffusion on Al(111). By

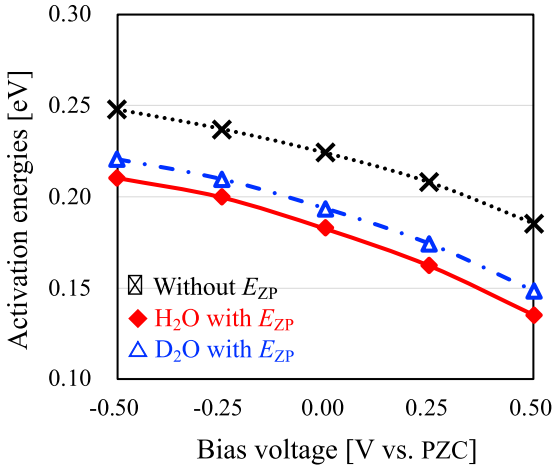

FIG. 6. Changes in the activation energies (E_a in eV) as a function of applied bias-voltage measured from PZC level (in V). Filled diamond and cross symbols, respectively, indicate E_a with and without correction of zero-point vibration energies (E_{ZP}) for H_2O, and open triangles denote E_a corrected by E_{ZP} of the heavy water (D_2O). The solid, dotted, and dash-dotted lines are intended to guide the eyes.

considering E_{ZP}, the results of E_a shown as diamond symbols decrease from those without the E_{ZP} correction. However, considering E_{ZP} does not qualitatively alter the bias-voltage dependence of E_a. According to the previous STM measurement [9,55], the positive bias-voltage increases the hopping rate for a single water molecule on the Pt surface. Since a decrease in E_a denotes an increase in the hopping rate, the present results are qualitatively consistent with the previous experiment. Besides, we calculated E_a for the heavy water (D_2O) shown as open triangles. Here, we determine E_{ZP} for the D_2O by using the deuterium mass for the hydrogen atoms. We found higher E_a for D_2O than that for the H_2O. This result denotes that the diffusion rate of D_2O becomes lower than that of the H_2O molecule, which is also consistent with the previous experiment findings [9,55]. Thus, E_{ZP} plays a role in considering the isotope effect on molecular diffusion. However, experimentally, the hopping rate for H_2O (or D_2O) dimer is increased by negatively increasing the bias voltage [9], which is not in agreement with the present results. This disagreement between theory and experiment comes from the absence of the interaction between the water molecules used in the present study. The previous study [20] has applied the conventional NEB calculation to not only simple water monomers and dimer diffusions but also a "waltzlike" diffusion mechanism on metal surfaces. The waltzlike diffusion is a two-step mechanism including rotation and donor-accepter exchange of the hydrogen-bond [19,20]. Computationally, comparing to the conventional method, the constant bias voltage might alter the details of the interaction between the H_2O molecules during the diffusion by the introduced ΔQ_e depending on the diffusion path. Therefore, we need to apply the constant-μ_e method presented in this study to such a complex diffusion process to reveal further details of the bias-dependent water diffusion on the surface in the future.

IV. SUMMARY

In summary, we demonstrated the realistic simulation of the bias-dependent diffusion of H_2O on the Al(111) and Pt(111) surfaces using NEB calculations within the constant-μ_e method. Our results for Al(111) showed that significant differences exist in the activation barrier energies and MEPs and that this depends on whether the applied bias voltage is positive or negative. In comparison, the FCP and GCSCF methods produced the same results within the computational accuracy. A comparison of the constant-μ_e and -N_e methods also showed that the constant-N_e method does not provide a good description of molecular diffusion under a bias voltage owing to the absence of excess charges introduced from the potentiostat. For the diffusion of H_2O and D_2O monomers on Pt(111), the present results are qualitatively consistent with the previous experimental findings. However, we need to consider the water dimer diffusion processes for further understanding of the water diffusion depending on the bias voltage. We expect the proposed method to find a wide variety of applications in the simulation of STM experiments and electrochemical reactions under constant electrode potentials.

ACKNOWLEDGMENTS

C.H. and M.O. thank Prof. O. Sugino for valuable discussions. This work was supported by MEXT as the "Program for Promoting Research on the Supercomputer Fugaku" (Fugaku Battery & Fuel Cell Project), Grant No. JPMXP1020200301. The computations were performed using the supercomputers of Research Center for Computational Science (Okazaki, Japan), Institute for Solid State Physics and Information Technology Center at the University of Tokyo, Flow provided by Nagoya university and Fugaku provided by the RIKEN Center for Computational Science.

[1] M. A. Henderson, Surf. Sci. Rep. **46**, 1 (2002).
[2] T. Mitsui, M. Rose, E. Fomin, D. F. Ogletree, and M. Salmeron, Science **297**, 1850 (2002).
[3] A. Michaelides, V. A. Ranea, P. L. De Andres, and D. A. King, Phys. Rev. Lett. **90**, 216102 (2003).
[4] S. Meng, E. G. Wang, and S. Gao, Phys. Rev. B **69**, 195404 (2004).
[5] S. Schnur and A. Groß, New J. Phys. **11**, 125003 (2009).
[6] J. Carrasco, A. Hodgson, and A. Michaelides, Nat. Mater. **11**, 667 (2012).
[7] H. Ogasawara, B. Brena, D. Nordlund, M. Nyberg, A. Pelmenschikov, L. G. M. Pettersson, and A. Nilsson, Phys. Rev. Lett. **89**, 276102 (2002).
[8] T. Utsunomiya, Y. Yokota, T. Enoki, and K.-I. Fukui, Chem. Commun. **50**, 15537 (2014).
[9] K. Motobayashi, L. Árnadóttir, C. Matsumoto, E. M. Stuve, H. Jónsson, Y. Kim, and M. Kawai, ACS Nano **8**, 11583 (2014).
[10] P. Hohenberg and W. Kohn, Phys. Rev. **136**, B864 (1964).
[11] W. Kohn and L. J. Sham, Phy. Rev. **140**, A1133 (1965).
[12] A. Michaelides, V. A. Ranea, P. L. de Andres, and D. A. King, Phys. Rev. B **69**, 075409 (2004).
[13] V. A. Ranea, A. Michaelides, R. Ramírez, P. L. de Andres, J. A. Vergés, and D. A. King, Phys. Rev. Lett. **92**, 136104 (2004).
[14] J. Li, Y. Li, S. Zhu, and F. Wang, Phys. Rev. B **74**, 153415 (2006).
[15] J. Li, S. Zhu, Y. Li, and F. Wang, Phys. Rev. B **76**, 235433 (2007).
[16] G. Mills, H. Jónsson, and G. K. Schenter, Surf. Sci. **324**, 305 (1995).
[17] G. Henkelman, B. P. Uberuaga, and H. Jónsson, J. Chem. Phys. **113**, 9901 (2000).
[18] G. Henkelman and H. Jónsson, J. Chem. Phys. **113**, 9978 (2000).
[19] C. Bertram, W. Fang, P. Pedevilla, A. Michaelides, and K. Morgenstern, Nano Lett. **19**, 3049 (2019).
[20] W. Fang, J. Chen, P. Pedevilla, X.-Z. Li, J. O. Richardson, and A. Michaelides, Nat. Commun. **11**, 1689 (2020).
[21] J. Matthiesen, J. O. Hansen, S. Wendt, E. Lira, R. Schaub, E. Lægsgaard, F. Besenbacher, and B. Hammer, Phys. Rev. Lett. **102**, 226101 (2009).
[22] V. A. Ranea, J. Chem. Phys. **137**, 204702 (2012).

[23] S. Karkare, L. Boulet, A. Singh, R. Hennig, and I. Bazarov, Phys. Rev. B **91**, 035408 (2015).
[24] T. B. Rawal, S. Hong, A. Pulkkinen, M. Alatalo, and T. S. Rahman, Phys. Rev. B **92**, 035444 (2015).
[25] A. Lozovoi, A. Alavi, J. Kohanoff, and R. Lynden-Bell, J. Chem. Phys. **115**, 1661 (2001).
[26] I. Tavernelli, R. Vuilleumier, and M. Sprik, Phys. Rev. Lett. **88**, 213002 (2002).
[27] W. B. Schneider and A. A. Auer, Beilst. J. Nanotechnol. **5**, 668 (2014).
[28] U. Benedikt, W. B. Schneider, and A. A. Auer, Phys. Chem. Chem. Phys. **15**, 2712 (2013).
[29] N. Bonnet, T. Morishita, O. Sugino, and M. Otani, Phys. Rev. Lett. **109**, 266101 (2012).
[30] R. Sundararaman, W. A. Goddard III, and T. A. Arias, J. Chem. Phys. **146**, 114104 (2017).
[31] T. Ikeshoji and M. Otani, Phys. Chem. Chem. Phys. **19**, 4447 (2017).
[32] R. Sundararaman, K. Letchworth-Weaver, and K. A. Schwarz, J. Chem. Phys. **148**, 144105 (2018).
[33] J. Haruyama, T. Ikeshoji, and M. Otani, J. Phys. Chem. C **122**, 9804 (2018).
[34] S. E. Weitzner, S. A. Akhade, J. B. Varley, B. C. Wood, M. Otani, S. E. Baker, and E. B. Duoss, J. Phys. Chem. Lett. **11**, 4113 (2020).
[35] K. Kano, S. Hagiwara, T. Igarashi, and M. Otani, Electrochim. Acta **377**, 138121 (2021).
[36] M. Otani and O. Sugino, Phys. Rev. B **73**, 115407 (2006).
[37] C. G. Broyden, J. Inst. Appl. Math. **6**, 222 (1970).
[38] R. Fletcher, Comput. J. **13**, 317 (1970).
[39] D. Goldfarb, Math. Comput. **24**, 23 (1970).
[40] D. F. Shanno, Math. Comput. **24**, 647 (1970).
[41] P. Pulay, J. Comput. Chem. **3**, 556 (1982).
[42] G. P. Kerker, Phys. Rev. B **23**, 3082 (1981).
[43] C. G. Broyden, Math. Comput. **19**, 577 (1965).
[44] P. Giannozzi, S. Baroni, N. Bonini, M. Calandra, R. Car, C. Cavazzoni, D. Ceresoli, G. L. Chiarotti, M. Cococcioni, I. Dabo *et al.*, J. Phys.: Condens. Matter **21**, 395502 (2009).
[45] P. Giannozzi, O. Andreussi, T. Brumme, O. Bunau, M. B. Nardelli, M. Calandra, R. Car, C. Cavazzoni, D. Ceresoli, M. Cococcioni *et al.*, J. Phys.: Condens. Matter **29**, 465901 (2017).
[46] D. Vanderbilt, Phys. Rev. B **41**, 7892 (1990).
[47] S. Popović, B. Gržeta, V. Ilakovac, R. Kroggel, G. Wendrock, and H. Löffler, Phys. Status Solidi A **130**, 273 (1992).
[48] AtomWork, https://crystdb.nims.go.jp/.
[49] J. P. Perdew, J. A. Chevary, S. H. Vosko, K. A. Jackson, M. R. Pederson, D. J. Singh, and C. Fiolhais, Phys. Rev. B **46**, 6671 (1992).
[50] I. Hamada, Phys. Rev. B **89**, 121103(R) (2014).
[51] D. Raczkowski, A. Canning, and L. W. Wang, Phys. Rev. B **64**, 121101(R) (2001).
[52] The first and the last images of the NEB calculation were prepared by the most stable adsorption structure at a bias U. Then the intermediate images were initialized using the interpolation scheme both for the geometry and charge.
[53] The sign of U is set as in the STM: A positive sample bias drives the electron injected into the sample and increases the Fermi energy with respect to the μ_{pzc}.
[54] T. Frederiksen, M. Paulsson, M. Brandbyge, and A.-P. Jauho, Phys. Rev. B **75**, 205413 (2007).
[55] K. Motobayashi, C. Matsumoto, Y. Kim, and M. Kawai, Surf. Sci. **602**, 3136 (2008).